Aeroelastic large eddy simulations using vortex methods: unfrozen turbulent and sheared inflow

Branlard, Emmanuel Simon Pierre; Papadakis, G.; Gaunaa, Mac; Winckelmans, G.; Larsen, Torben J.

Published in:
Journal of Physics: Conference Series

Link to article, DOI:
10.1088/1742-6596/625/1/012019

Publication date:
2015

Document Version
Publisher's PDF, also known as Version of record

Aeroelastic large eddy simulations using vortex methods: unfrozen turbulent and sheared inflow

2015 J. Phys.: Conf. Ser. 625 012019

(http://iopscience.iop.org/1742-6596/625/1/012019)

Journal of Physics: Conference Series **625** (2015) 012019 doi:10.1088/1742-6596/625/1/012019

Aeroelastic large eddy simulations using vortex methods: unfrozen turbulent and sheared inflow

E. Branlard[1], G. Papadakis[2], M. Gaunaa[1], G. Winckelmans[3], T. J. Larsen[1]

[1] Department of Wind Energy, Technical University of Denmark, Frederiksborgvej 399, 4000 Roskilde, Denmark
[2] NTUA, School of Mechanical engineering, Greece
[3] Institute of Mechanics, Materials and Civil Engineering (iMMC), Université catholique de Louvain, Belgium

E-mail: ebra@dtu.dk

Abstract. Vortex particles methods are applied to the aeroelastic simulation of a wind turbine in sheared and turbulent inflow. The possibility to perform large-eddy simulations of turbulence with the effect of the shear vorticity is demonstrated for the first time in vortex methods simulations. Most vortex methods formulation of shear, including segment formulations, assume a frozen shear. It is here shown that these formulations omit two source terms in the vorticity equation. The current paper also present unfrozen simulation of shear. The infinite support of the shear vorticity is accounted for using a novel approach relying on a Neumann to Dirichlet map. The interaction of the sheared vorticity with the wind turbine is shown to have an important impact on the wake shape. The obtained wake shape are closer to the one obtained using traditional computational fluid dynamics: Results with unfrozen shear do not have the severe upward motion of the wake observed in vortex methods simulation with frozen shear. The interaction of the shear and turbulence vorticity is shown to reduce the turbulence decay otherwise observed. The vortex code implemented is coupled to an aeroelastic code and examples of aeroelastic simulations under sheared and turbulent inflow are presented.

1. Introduction

Conventional aeroelastic codes use the Blade Element Momentum method (BEM) to determine the induced velocities and the aerodynamic loads at the blade. A precomputed synthetic velocity component is added to the induced velocities to include the effect of turbulence [1]. The turbulent field, referred to as a "turbulent box", convects with the free-stream velocity under the assumption of Taylor's hypothesis of frozen turbulence [2].

Aeroelastic simulations have also been performed using higher order aerodynamic tools such as vortex methods [3] and traditional Computational Fluid Dynamics (CFD) [4], at a successively increasing computational cost. The methods have been applied to steady inflow conditions. Vortex methods have been recently used to perform non-aeroelastic Large Eddy Simulations (LES) of wind turbines by Chatelain et al. [5]. The current study is conducted by performing aeroelastic LES of wind turbines using vortex methods and by further examining the inclusion of shear in the method.

The paper is structured as follows. The theoretical and computational models are presented in a first section. The different components of the implementation are then studied in more

detail. The final part presents combined analyses of the different components.

2. Model and computational setup

2.1. Problem definition

A wind turbine operating under sheared and turbulent inflow is considered. The shear and the turbulence are assumed to be given at a distance upstream of the turbine, while the process responsible for their generation is not modelled. The turbulence is assumed to be generated by an upstream mask of finite cross section upstream. The layout is sketched in Figure 1. The

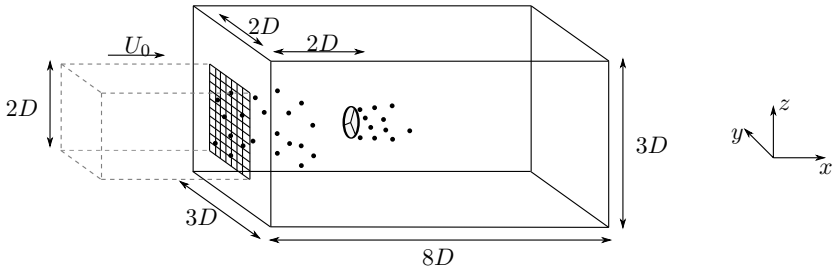

Figure 1: Computational setup. Turbulent vortex particles generated by a mask (represented by a grid) are inserted at each time step. The wind turbine wake is modeled with vortex particles. The domain is filled with particles (not shown) representing the shear vorticity, also inserted at each time step.

incompressible Navier-Stokes equation in vorticity formulation and in Lagrangian coordinates $\boldsymbol{X}(\boldsymbol{\xi}, t)$, with $\boldsymbol{X}(\boldsymbol{\xi}, 0) = \boldsymbol{\xi}$, takes the form:

$$\frac{d\boldsymbol{\omega}}{dt}(\boldsymbol{X}, t) = [\boldsymbol{\nabla}\boldsymbol{u}(\boldsymbol{X}, t)] \cdot \boldsymbol{\omega}(\boldsymbol{X}, t) + \nu\nabla^2\boldsymbol{\omega}(\boldsymbol{X}, t), \qquad \frac{d\boldsymbol{X}}{dt}(\boldsymbol{\xi}, t) = \boldsymbol{u}(\boldsymbol{X}, t) \tag{1}$$

where $\boldsymbol{u}$ is the flow velocity, ν is the fluid viscosity, and $\boldsymbol{\omega} = \nabla \times \boldsymbol{u}$ is the vorticity. Of the wind turbine, only the blades are modelled and a lifting line approach is used: The blades are represented by a line of bound vorticity which shed and trailed vorticity in the wake (see e.g. [6]). The entire system of the fluid and the turbine is thus modelled in a unified vorticity formulation.

2.2. Vorticity inversion and Helmholtz decomposition

For most physical applications, a velocity field $\boldsymbol{u}$ can be written according to the Helmholtz decomposition [7]: $\boldsymbol{u} = \boldsymbol{U}_0 + \boldsymbol{u}_\omega + \boldsymbol{u}_\phi$ where $\nabla \times \boldsymbol{U}_0 = 0$, $\nabla \cdot \boldsymbol{U}_0 = 0$, $\nabla \cdot \boldsymbol{u}_\omega = 0$ and $\nabla \times \boldsymbol{u}_\phi = 0$. The divergent free component is written as function of a vector potential $\boldsymbol{\psi}$ as $\boldsymbol{u}_\omega = \nabla \times \boldsymbol{\psi}$. Choosing the gauge $\nabla \cdot \boldsymbol{\psi} = 0$, the definition $\boldsymbol{\omega} = \nabla \times \boldsymbol{u}$ leads to $\Delta\boldsymbol{\psi} = -\boldsymbol{\omega}$. For incompressible flows $\boldsymbol{u}_\phi$ accounts for boundary conditions. In absence of boundaries and for a flow occupying the entire space $\boldsymbol{u}_\phi = 0$. In an unbounded space and in the absence of boundaries, the velocity can be retrieved from the vorticity field using the Biot-Savart law:

$$\boldsymbol{u}_\omega(\boldsymbol{x}, t) = \int_D \boldsymbol{K}(\boldsymbol{x} - \boldsymbol{x'}) \times \boldsymbol{\omega}(\boldsymbol{x'}, t)\, d\boldsymbol{x'}\ , \qquad \boldsymbol{K}(\boldsymbol{r}) = -\frac{\boldsymbol{r}}{4\pi\, r^3} \tag{2}$$

where the integral is taken over $D = D_\omega$, with D_ω the support of vorticity, possibly infinite. If one restricts the integral to a smaller domain $D = D_{\text{in}}$, the contribution from the vorticity outside of the domain is accounted for by means of a Neumann to Dirichlet map (or generalized Helmholtz decomposition) which ensures the continuity of tangential and normal velocity at the domain interface ∂D_{in} [8]. The velocity field is then written $\boldsymbol{u} = \boldsymbol{U}_0 + \boldsymbol{u}_\omega + \boldsymbol{u}_{\text{ext}}$ with

$$\boldsymbol{u}_{\text{ext}}(\boldsymbol{x}) = \int_{\partial D_{\text{in}}} \left[-\boldsymbol{K}(\boldsymbol{x} - \boldsymbol{x'})\, u_n(\boldsymbol{x'}) + \boldsymbol{K}(\boldsymbol{x} - \boldsymbol{x'}) \times \boldsymbol{u}_\tau\right]\, d\boldsymbol{x'} \tag{3}$$

where, u_n is the component of the input field normal to ∂D_{in} such that $u_n = \boldsymbol{u} \cdot \boldsymbol{n}$, with $\boldsymbol{n}$ pointing towards the interior of the domain, and $\boldsymbol{u}_\tau = \boldsymbol{n} \times \boldsymbol{u}$. The gradient $\boldsymbol{\nabla u}_{\text{ext}}$ is directly obtained from the expression of $\boldsymbol{u}_{\text{ext}}$. In the current study D_{in} represents the computational domain and it is assumed for simplicity that the contribution from $\boldsymbol{u}_{\text{ext}}$ is time invariant.

2.3. The numerical tool

Equation 1 is solved using a vortex particle approximation [9]. The vorticity field is written as a sum of particle strengths $\boldsymbol{\alpha}_p = \int_{V_p} \boldsymbol{\omega}\, dV$ weighted by a local function ζ, as

$$\boldsymbol{\omega}(\boldsymbol{x}, t) \approx \boldsymbol{\omega}_\alpha(\boldsymbol{x}, t) = \sum_p \zeta(|\boldsymbol{x} - \boldsymbol{x}_p|)\, \boldsymbol{\alpha}_p(t) \tag{4}$$

where $\boldsymbol{x}_p$ is the position of the particle and V_p a volume attributed to the particle. In the present study a second order exponential function is used for ζ.

The velocity and its gradient in the domain can be determined in two ways. Both approaches are tested in this study. Inserting Equation 4 into Equation 2, the particle positions are used as quadrature points and the Biot-Savart integral becomes a summation over the particles. A second order multipole tree algorithm is used for a fast evaluation of the summation [10]. This will be here referred to as the "mesh-free" method and was added to the in-house solver *Omnivor* since its previous description [11]. Alternatively, the vorticity carried by the particles can be projected onto a grid and the velocity is then retrieved using a Poisson solver (Particle Mesh Methods): solving $\nabla^2 \boldsymbol{\psi} = -\boldsymbol{\omega}$ for $\boldsymbol{\psi}$ and getting $\boldsymbol{u} = \nabla \times \boldsymbol{\psi}$, or solving $\nabla^2 \boldsymbol{u}_\omega = -\nabla \times \boldsymbol{\omega}$ for $\boldsymbol{u}$ directly. The second order Poisson solver, *Yaps*, developed at NTUA is used [12] and is coupled to the *Omnivor* library. In order to facilitate performance of the Poisson solver, the method of local corrections is applied [13] together with a domain decomposition method described in [14]. Regardless of the approach used, particles are convected using a first-order forward Euler scheme. Redistribution (re-meshing) of the particles on a regular lattice every few time-steps is performed to ensure the coverage of the space and retain accuracy [15]. Even in the "mesh-free" formulation, an underlying grid and computational domain is thus defined.

The vortex code *Omnivor* was coupled [11] to the aero-servo-elastic code *HAWC2* [16] using a strong coupling: At each sub-iteration of the structural solver new aerodynamic loads on the lifting-line are computed by the vortex code based on the new blade position using an iteration procedure on the bound and near-wake circulation [6] and using a form of the Beddoes-Leishman dynamic stall model [17]; at the end of a time step Equation 1 is solved for the free vorticity.

2.4. Viscosity and LES

For the high Reynolds number considered here ($\text{Re} \approx [10^5 - 10^7]$), the omission of the diffusion associated with the molecular viscosity can be justified. Yet, the inclusion of turbulence calls for an account of viscous effects. In the current study, the effects of the smaller scales is modelled by limiting the amount of stretching and by using a low-order kernel in the re-meshing scheme to act as a subgrid-scale (SGS) filter [18, p. 140]. The λ_1 kernel is here used [15]. This approximation was used in a previous study by the authors [19]. The approach is convenient when the mesh-free method is used. Indeed, the computation of viscous terms [20] or SGS models [21] is possible by integral approximation of the differential operators but the method can be computationally expensive for large amount of particles. Using the Poisson-solver approach though, finite difference tools are directly available on the grid and can be used for computing the diffusion and different sub-grid scale models [5, 15]. Considering the coupling with the *Yaps* Poisson solver the finite-difference sub-grid scale models will be tried in the near future.

2.5. The simulation setup
The computational domain used in the present study has dimensions $8D \times 3D \times 3D$ as shown in Figure 1. The three-bladed Nordtank 500kW stall regulated wind turbine located at one of DTU Wind Energy's test sites is modelled. The turbine diameter is $D = 2R = 41$m and it rotates at the constant speed $\Omega = \dot{\theta} = 27.1$ RPM. The free-stream velocity is chosen as $U_0 = 7.5\text{m.s}^{-1}$ and the tip-speed ratio is then $\lambda = 7.7$. The shear is assumed linear of slope $du_s/dz = 0.079\text{s}^{-1}$ so that the free-stream velocity at the blade tip varies between 6 and 9m.s^{-1}. The domain consists of a grid of $256 \times 96 \times 96$ cells resulting in 2.4M particles. Re-meshing is performed every 10 time steps. The time step chosen is $dt = 0.086$s ($d\theta = 14°$), while the total simulation time is 300s. Particles exiting the domain are discarded but a hybrid wake approach could be used [22].

3. Separate analysis of the different models involved

3.1. Accuracy of the numerical tools
The accuracy of vortex particle methods depends to a large extent on the determination of the velocity $\boldsymbol{u}$ and deformation $[\boldsymbol{\nabla u}].\boldsymbol{\omega}$ from the distribution of vorticity. The accuracy of both the mesh-free Biot-Savart law and the Poisson solver approaches are studied by comparison with the analytical formulae of the Hill's spherical vortex [23, 24]. The particles are initialized using the analytical vorticity value on a regular grid of spacing h/a where a is the radius of the Hill's sphere. The domain extends from $-1.2a$ to $1.2a$ is all directions. The velocity is then computed by the two methods on two control volumes: one entirely located inside the sphere and one crossing the sphere surface. Both volumes are made of 1000 control points that remain unchanged for the different grid spacings tried. The second control volume is more challenging since the vorticity experiences a discontinuity at the sphere boundary. The mean relative error between the numerical and analytical velocity and deformation on the two control volumes are shown in Figure 2. The Poisson solver uses a grid of the same spacing as the particle spacing. Different grid spacing h were used, the lowest grid resolution corresponding to 2000 particles and the highest to 14M. Resolutions up to 628M particles were also tried. Both methods are seen to be second order as expected. Better performance of the Poisson solver was observed in the determination of the velocity. For the mesh-free approach, the accuracy can easily be improved by using higher order 3D regularization kernels ζ [25, 26] as long as the vorticity distribution has sufficient continuous derivatives [27]. For the Poisson solver, both the order of the solver and the order of the differentiation scheme are important. Since the solution of the Poisson problem highly depends on the quality of the information projected on the grid, it is usually recommended to use more than one particle per cell to increase accuracy and limit diffusion during the re-meshing procedure. These will be considered in future studies.

3.2. Representation of shear
Inviscid flows are used in this section but the results can be extended to viscous flows.

Shear only A vertical shear profile $\boldsymbol{u}_s = U_s(z)\boldsymbol{e}_x$ is associated to a vorticity profile $\boldsymbol{\omega}_s = \frac{dU_s}{dz}\boldsymbol{e}_z$ and the gradient of the velocity field is $[\boldsymbol{\nabla U}_s] = \frac{dU_s}{dz}\,\boldsymbol{e}_y \otimes \boldsymbol{e}_z$. The vorticity equation for a shear flow is directly obtained from Equation 1 as:

$$\frac{\partial \boldsymbol{\omega}_s}{\partial t} + [\boldsymbol{\nabla \omega}_s] \cdot \boldsymbol{U}_s = [\boldsymbol{\nabla U}_s] \cdot \boldsymbol{\omega}_s \qquad \text{(Unfrozen Shear - Shear only)} \tag{5}$$

All three terms are zero for a uniform and steady shear flow.

Shear and additional vorticity Another source of vorticity is here assumed to be present in the flow such that the total vorticity is $\boldsymbol{\omega} = \boldsymbol{\omega}_s + \tilde{\boldsymbol{\omega}}$ and the total velocity is $\boldsymbol{u} = \boldsymbol{U}_s + \tilde{\boldsymbol{u}}$. The

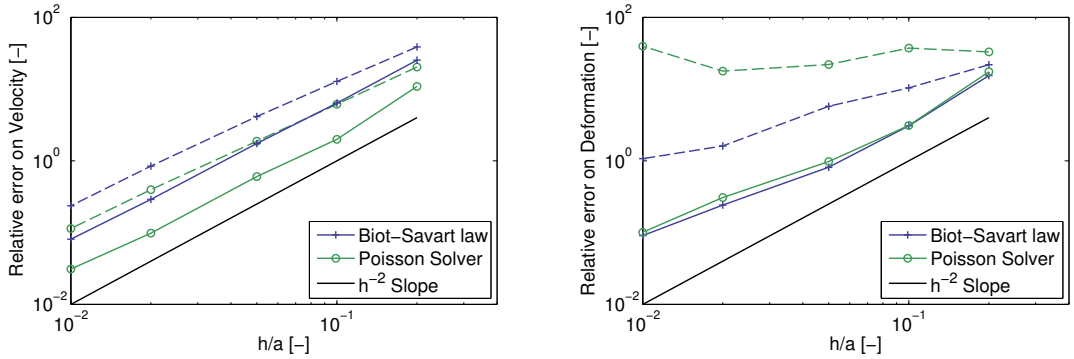

Figure 2: Accuracy of the current particle method using the Biot-Savart law or the Poisson solver by comparison with the analytical solution from the Hill's vortex. Relative error in velocity (left) and deformation (right). The errors were evaluated in a domain inside the Hill's vortex (plain lines), and in a domain surrounding part of the boundary of the vortex (dashed lines). The latter present more challenges due to the discontinuity of the vorticity across the boundary.

.

evolution of the total vorticity is given in Equation 1, written again below:

$$\frac{\partial \boldsymbol{\omega}}{\partial t} + [\boldsymbol{\nabla \omega}] \cdot \boldsymbol{u} = [\boldsymbol{\nabla u}] \cdot \boldsymbol{\omega} \qquad \text{(Unfrozen Shear - Full interaction)} \tag{6}$$

Frozen shear The term "frozen shear" will be used to denote the case where the additional vorticity does not affect the shear vorticity. Developing the expressions of $\boldsymbol{u}$ and $\boldsymbol{\omega}$ in Equation 6, and using the fact that Equation 5 holds if the shear is frozen, leads to:

$$\frac{\partial \tilde{\boldsymbol{\omega}}}{\partial t} + [\boldsymbol{\nabla}\tilde{\boldsymbol{\omega}}] \cdot (\boldsymbol{U}_s + \tilde{\boldsymbol{u}}) = ([\boldsymbol{\nabla U}_s] + [\boldsymbol{\nabla}\tilde{\boldsymbol{u}}]) \cdot \boldsymbol{\omega} - [\boldsymbol{\nabla \omega}_s] \cdot \tilde{\boldsymbol{u}} + [\boldsymbol{\nabla}\tilde{\boldsymbol{u}}] \cdot \boldsymbol{\omega_s} \qquad \text{(Frozen Shear)} \tag{7}$$

Frozen shear - Erroneous approach In all vortex methods wind turbine simulations known to the authors, the wind shear is assumed frozen and included as part of the "free-stream" [28, 29, 22]. In vortex particle simulations, the term $[\boldsymbol{\nabla U}_s]$ is added to the gradient $[\boldsymbol{\nabla}\tilde{\boldsymbol{u}}]$ in order to include the deformations due to the shear. In vortex segments simulations this term is automatically included since the vortex segments are convected as material elements. For such particle or segment simulation the vorticity equation solved for is:

$$\frac{\partial \tilde{\boldsymbol{\omega}}}{\partial t} + [\boldsymbol{\nabla}\tilde{\boldsymbol{\omega}}] \cdot (\boldsymbol{U}_s + \tilde{\boldsymbol{u}}) = ([\boldsymbol{\nabla U}_s] + [\boldsymbol{\nabla}\tilde{\boldsymbol{u}}]) \cdot \tilde{\boldsymbol{\omega}} \qquad \text{(Frozen Shear - Erroneous)} \tag{8}$$

Comparison of Equation 7 and 8 reveals that most vortex code implementations with frozen shear omit two terms. The two additional terms are easily implemented in a vortex particle simulation. The term $[\boldsymbol{\nabla \omega}_s] \cdot \boldsymbol{u}$ is zero for a linear shear but the term $[\boldsymbol{\nabla}\tilde{\boldsymbol{u}}] \cdot \boldsymbol{\omega}_s$ is non negligible. The consequence of this omission for wind turbine wakes will be discussed in subsection 4.2.

Numerical implementation for Unfrozen Shear A novel approach to account for the shear vorticity and its possible interaction with the additional vorticity is described in the following. The shear vorticity contained within the computational domain is interpolated onto vortex particles. Since the shear vorticity has an infinite support, the external map from Equation 3 is used to account for the velocity $\boldsymbol{u}_{\text{ext}}$ and gradient $[\boldsymbol{\nabla u}_{\text{ext}}]$ due to the vorticity outside of the computational domain. In a time-stepping simulation, the "shear" vortex particles convecting

outside of the domain at the outlet are discarded whereas new particles are inserted at the inlet. The particles are inserted on a regular grid of spacing h in the $y-z$ plane of the inlet. The validation of the whole procedure, with and without time-stepping, is shown in Figure 3 for a step shear and a linear shear. The contribution of the external map from Equation 3 is crucial to reconstruct the exact shear and allow long term simulations with the proper deformation of the vortex particles. The method can be applied to any kind of shear with the same accuracy since the developments of subsection 2.2 are exact. The only approximation comes in the evaluation of the Biot-Savart and surface map integrals. In the current study, the surface map integral is computed using point sources and point vortices which result in loss of accuracy close to the boundary D_{in}. Small instabilities were observed at the end of the computational domain due to this point-wise approximation. The rest of the domain is not seen to be significantly affected by these instabilities as seen in Figure 3. The use of piecewise constant surface panels and the account of the principal value of the integral at the surface itself will increase the accuracy.

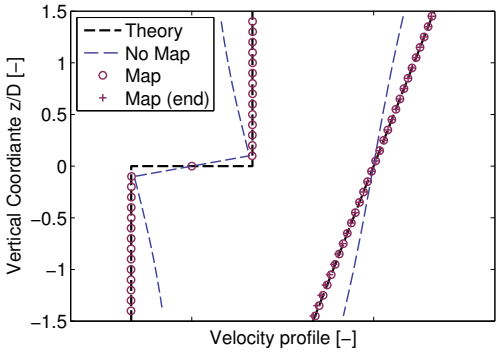

Figure 3: Modelling of shear using vortex particles. Velocity profiles obtained at the center of the domain for a step shear and a linear shear. The inclusion of the surface map from Equation 3 is crucial. The curved labelled "(end)" is extracted at the end of the simulation. The shear is seen to be conserved with time despite the numerical error that could be introduced by the re-meshing, numerical stretching and convection.

3.3. Representation of turbulence using vortex particles

The approach used by Chatelain et al. [5] is followed: A synthetic isotropic turbulent velocity field is computed prior to the simulation using the Mann model [30]; the velocity field is smoothly clipped on the side, by multiplication with a function that smoothly drops to zero, to avoid strong vortex lines at these locations; the vorticity of the field is computed and interpolated onto vortex particles; at the initial time step the domain is filled with these "turbulent" vortex particles while more particles are inserted at each time-step at the inlet of the domain. The method was previously used in the literature [31, 32, 33] and recently applied by the authors to study the impact of a wind turbine on turbulence [19]. More details can be found in these references. Instead of clipping the turbulent vorticity field, an external map could also be used but the surface integral would need to be evaluated at each time step since the flow on the surface is unsteady.

The vorticity obtained from the particle approximation is represented in the right of Figure 4 for the initial and final time steps. The spectra of the velocity fields are shown in the left of Figure 4. The evolution of the turbulence intensity can be seen in Figure 6. The current particle approximation was estimated to have a cut-off frequency of about $f_{\text{cut}} \approx U_0/10h$ [19]. This explains the differences between the input Mann spectrum and the "Frozen" spectrum obtained by purely convecting the particle turbulent field using the free-stream velocity and without

allowing it to deform. When the particle field is allowed to deform ("Unfrozen Turbulence"), the turbulent kinetic energy k_t decays with the distance from the insertion point. The same behavior was found in CFD simulations where turbulence is inserted as body forces [34]. In the presence of viscous forces the decay of k_t behind a mask is expected if there is no driving force to sustain turbulence [35]. Batchelor and Townsend [36] observed a linear decay of the kinetic energy independently of the viscosity value. This is consistent with the theory from Kármán and Howarth [37] that obtained the decay as $\frac{dk_t}{dt} = -10\nu\frac{k_t}{\lambda^2}$, where λ denotes the representative length scale, when λ satisfies $\lambda^2 \propto \nu/\sqrt{k_t}$. More advanced turbulence decay models can be found e.g. in the work of Thormann and Meneveau [38]. The reproduction of the early linear decay seen in the curve labelled "No Shear" in Figure 6 confirms the validity of the current model. The other curves of the figure are discussed in subsection 4.1. More analyses on the turbulence modelling were performed by the authors in [19].

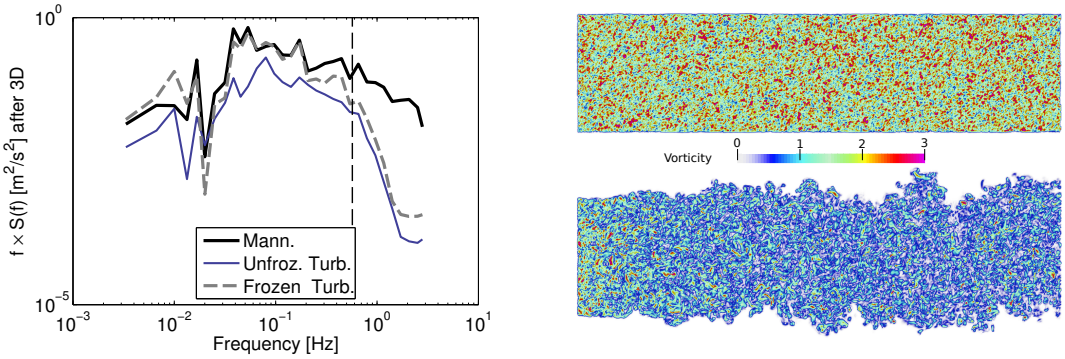

Figure 4: Statistics of the turbulent velocity fields represented using vortex particles. Left: comparison of the original velocity spectrum with the ones obtained from the particle approximation. The unfrozen spectrum is shown at $x = 0$, after the turbulence has evolved over 2 diameters. Right: Vorticity for frozen turbulence (top) and unfrozen decaying turbulence (bottom). $x \in [-2D, 6D]$

3.4. Wind turbine wake simulation using particles

The *Omnivor* library in its segments wake formulation was previously validated against BEM codes, actuator-line and actuator-disk (AD) simulations results and measurements [11, 39]. The principle of the vortex segment wake formulation used is similar to the one described for the *AWSM* code [6]. The particle formulation simply consists in converting the wake segments into vortex particles. The bound segments may also be temporarily converted to particles. The particle wake formulation is here validated against the segment wake formulation.

Vortex particles can be seen as lower order vortex elements compared to vortex segments. As a first step, the difference between the velocity induced by a vortex segment and a vortex particle is investigated. A given vortex segment of length l and intensity $\mathbf{\Gamma}$ is modeled using a distribution of n equally spaced vortex particles of intensity $\boldsymbol{\alpha} = \mathbf{\Gamma} l/n$. The velocity field from the segment or the collection of particles is evaluated on a surface described by h = constant, where h is the minimum distance to the segment. The maximum relative error on this surface for different values of h and n is shown in the left of Figure 5. The mean error was found to be about 2.5 lower than the maximum error.

The circulation along the span of the wind turbine blade for a simulation under uniform inflow with a vortex segment wake and with a particle wake is shown in the right of Figure 5. The agreement between the two cases validates the implementation of the particle wake method.

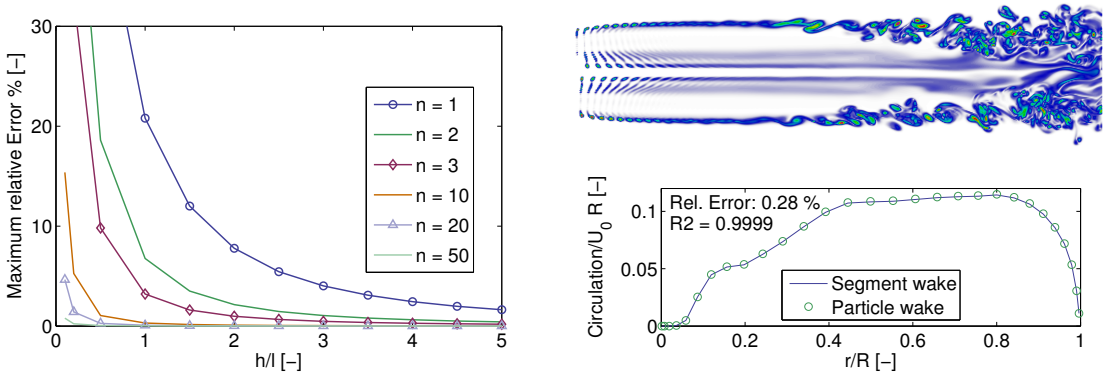

Figure 5: Comparison of segment and particle formulations. Left: error in the velocity field surrounding a vortex filament when represented using a distribution of n particles. Bottom-Right: Circulation along the blade at the end of the simulation using a vortex segment wake or a particle wake. Top-Right: vorticity values obtained from the particle simulation ($x \in [0D; 6D]$).

4. Combined analyses

4.1. Combination of shear and turbulence

It was seen in subsection 3.3 that the "unfrozen" turbulence tends to loose energy progressively as the eddies evolve away from the mask where they had been generated. The inclusion of shear is expected to sustain the turbulence. Shear and turbulence particles are here inserted as described individually in subsection 3.2 and subsection 3.3. When combining shear and turbulence, the velocities on the boundary ∂D_{in} will not be exactly the ones from the undisturbed shear. This is clear at the inlet and outlet of the turbulence but also on all other boundaries due to the induced velocities of the turbulence vortex particles on ∂D_{in} and due to the interaction between the shear and turbulence particles which may affect the strength of the shear particles. The difference between the unsteady velocity at the boundary and the steady state shear velocities are expected to be of second order and they are here omitted for simplicity. As seen in Equation 3, the errors involved would decrease in $1/r^2$ away from the boundaries, and an extension of the computational domain would thus reduce the error involved. No visible differences was observed using a lateral extent of 5D instead of 3D. Since meandering occurs, some shear particles might exit the domain on one side of the domain and holes may be created on the other side. Shear vortex particles are also inserted on the sides of the domain when such holes are detected. At the inlet, the shear particles are inserted as described in subsection 3.2: More shear vorticity is inserted where the wind velocity is higher. This approach is not followed for the turbulence as the turbulent particles are inserted with the free-stream. Further, the turbulence box used to generate the vortex particles is isotropic and it does not account for an inherent shear. The influence of these two limitations will be investigated in the future.

The evolution of the turbulence intensity across the domain is shown in Figure 6 for different cases. All simulations corresponds to "unfrozen turbulence". It is observed in the figure that the frozen shear does not significantly affect the turbulence kinetic energy which is seen to decay in the same proportion as the non-sheared case. On the other hand, the account for the full interaction is seen to reduce the decay and a trend towards a stabilisation of the turbulent kinetic energy can be foreseen. Analysis of the velocity profiles revealed that the shear slope was reduced when the full interaction was allowed. The turbulence extracts energy from the shear and tends to homogenize the profile. Troldborg et al. performed CFD simulations with prescribed linear shear and insertion of turbulence in an upstream plane of the domain [40]. In one of their test cases, the boundary condition consisted in artificially prescribing the velocity on the lower and higher boundary. This situation can be linked to the one used here where

the surface map is assumed constant. The authors observed that the inclusion of shear was sustaining turbulence and constant statistical properties of turbulence were obtained [40]. The current results are not as pronounced but the difference between the uniform and sheared inflow cases follow the same trends as their results. The fact that a decay occurs in the unfrozen shear case reveals inconsistencies between the numerical model and the input field. Future work will address this issue in order to obtain a sustained turbulence field throughout the domain in the presence of shear. This can be done by recirculating the turbulence field in a fashion similar to the study of Troldborg et al. [40] or by adjusting the parameters of the input turbulence box.

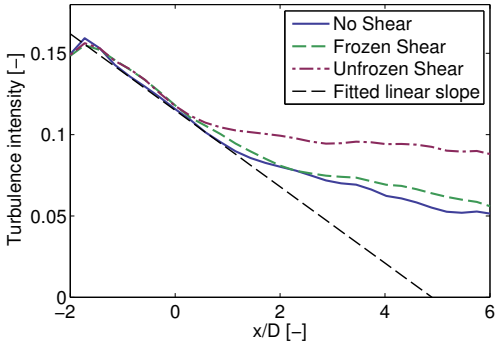

Figure 6: Evolution of the turbulence intensity with the distance from the turbulence insertion point. Accounting for the interaction between the shear and turbulence ("unfrozen shear") is seen to increase the turbulence intensity.

4.2. Combination of shear and wind turbine

Simulations of the Nordtank wind turbine are here presented for three cases: "Frozen Shear - Erroneous", "Frozen Shear", and "Unfrozen Shear". Vorticity contours for the "Frozen Shear - Erroneous" and "Unfrozen Shear" cases are shown in Figure 7. The wake shape for the case "Frozen Shear" is also shown on the figure. Results from the "Frozen Shear - Erroneous" case, in the top of Figure 7, are consistent with vortex segments simulations performed without the inclusion of the shear vorticity [29]. In the current study, it is seen that the interaction between the shear vorticity and the turbine has an important impact on the wake shape. The wake does not have such a significant upward motion when the full interaction is included. This result is consistent with CFD simulations [41]. The cancellation of the longitudinal vorticity of the wake induced by the shear and the longitudinal vorticity of the shear induced by the wake is likely to be the source of this result. It can be proven using a simple vortex model [42]. For the current simulation, the omission of this interaction leads to an overestimation of 4% of the power and 1% of the thrust. The comparison between the two frozen shear cases reveals the importance of the additional terms of Equation 7: Less upward motion of the wake is found and the wake shape compare better with the full-interaction case.

4.3. Aeroelastic LES of wind turbine with shear and turbulence

A proof of concept of the applicability of the different models to aeroelastic wind turbine simulations is presented here using the *HAWC2* and *Omnivor* tools. Turbulent simulations with different shear modelling are run. The simulation time for the full unfrozen case, was 7h30 with 160 CPUs using the tree-code algorithm. A total of 1h was spent in the iterative interaction with the structural code. Many future optimizations of the code are yet possible

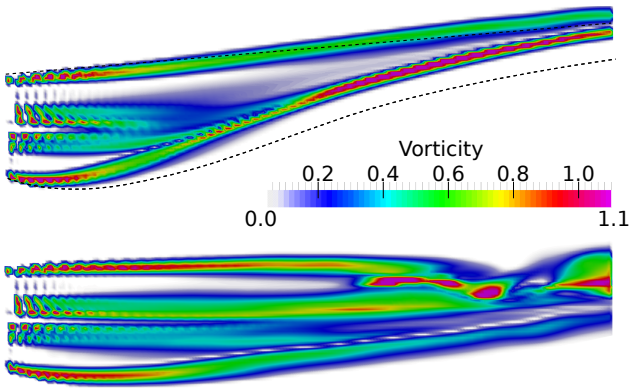

Figure 7: Vorticity contours in the wake of the turbine ($x \in [0D, 6D]$) for the case "Frozen Shear - Erroneous" (top) and "Unfrozen Shear - Full interaction" (bottom). The black dashed lines represent the wake shape for the correct "Frozen Shear" simulation (Equation 7). The interaction between the shear vorticity and the turbine has an important impact on the wake shape. Implementing the correct frozen shear equation improves the results but not enough to reach the results of the full interaction.

since new bottlenecks appeared in this study. Further speed up will be obtained by using the Poisson solver and by optimizing the re-meshing procedure (accounting for 30min here). The simulation time is roughly half the time of a typical CFD LES simulation with similar resolution at the rotor. Results are shown in Figure 8. The vertical lines corresponds to values obtained using the BEM aerodynamic module of *HAWC2* without turbulence. Both the BEM and vortex code predicts a reduction of loads and power when shear is present for the simulated operational conditions. Unfreezing the shear is seen to reduce the power mean value but increases its standard deviation. Little impact is seen on the flap-wise moment. Further investigations will be the topic of future work.

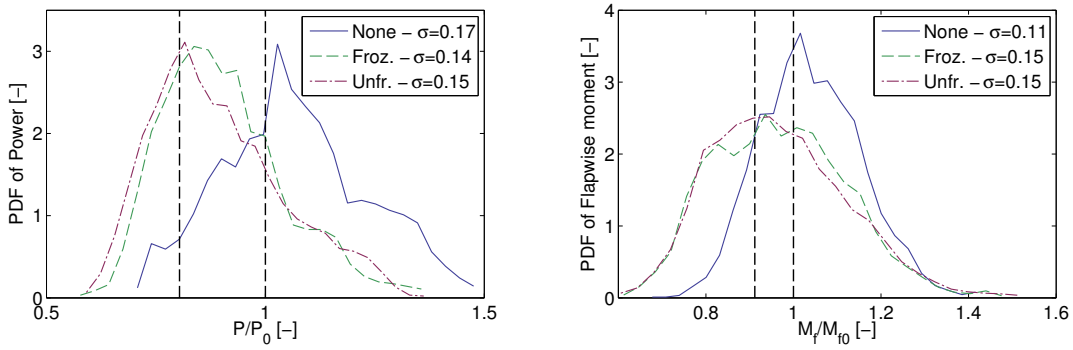

Figure 8: Probability density functions of power and flap-wise moments for turbulent aeroelastic simulations perform using the vortex code coupled with *HAWC2* under different shear conditions: no shear, frozen shear, unfrozen shear. The turbulence intensity is TI = 12% (see Figure 6 at $x = 0$). Vertical lines represent BEM value for TI = 0%, $P_0 = 148$kW, $M_{f,0} = 1.36$kNm. Unfreezing the shear is seen to reduce the power but has little influence on the flapwise moment.

5. Conclusions

Vortex particle methods were applied to turbulence, shear, a wind turbine and the combinations of these cases. For the first time, a Neumann to Dirichlet map was used to account for the

vorticity outside of the domain in the modelling of shear. The interaction of the shear and turbulence vorticity was seen to avoid the decay of turbulent kinetic energy. If shear is present but the interaction is not a two-way interaction, the decay occurs. It was shown that most vortex methods implementation of frozen shear were lacking two terms in the vorticity equation. The inclusion of these two terms reduces the upward motion of the wake in a sheared flow. The full interaction of the shear and the wind turbine vorticity further reduces this upward motion. Solving for the full interaction appeared of importance both for the wake shape and the loads. The possibility to perform aeroelastic simulations of wind turbine under sheared and turbulent conditions was demonstrated. It is the first time, known to the authors, that fully coupled lifting-line aeroelastic simulations including shear and turbulence have been performed. Future work should address the possibility to include unsteady boundary conditions in the method, more consistent SGS models, and further investigate the different interactions of vorticity.

Acknowledgments

The work was funded by the Danish Council for Strategic Research (DSF), under contract 2104-09-0026, Center for Computational Wind Turbine Aerodynamics and Atmospheric Turbulence. The computational cluster was provided by DCSC and the DTU central computing facility.

References

[1] G. C. Larsen, H. A. Madsen, K. Thomsen, and T. J. Larsen. Wake meandering. *Wind Energy*, 11(4):377–395, 2008.
[2] G. I. Taylor. The spectrum of turbulence. *Proceedings of The Royal Society of London Series A-Mathematical And Physical Sciences*, 164(A919):0476–0490, 1938.
[3] V. A. Riziotis, D. I. Manolas, and S. G. Voutsinas. Free-wake aeroelastic modelling of swept rotor blades. *European Wind Energy Conference and Exhibition 2011, EWEC 2011*, 2011.
[4] J. C. Heinz. *Partitioned Fluid-Structure Interaction for Full rotor computations using CFD*. PhD thesis, Technical University of Denmark, 2013.
[5] P. Chatelain, S. Backaert, G. Winckelmans, and S. Kern. Large eddy simulation of wind turbine wakes. *Flow Turbulence And Combustion*, 91(3):587–605, 2013.
[6] A. van Garrel. Development of a wind turbine aerodynamics simulation module. Technical Report ECN-C–03-079, ECN, 2003.
[7] S. M. Richardson and A. R. H. Cornish. Solution of three dimensional incompressible flow problems. *Journal of Fluid Mechanics*, 82:pp. 309–319, 1977.
[8] G. Papadakis and S. G. Voutsinas. In view of accelerating CFD simulations through coupling with vortex particle approximations. *Journal of Physics: Conference Series*, 524(1):012126, 2014.
[9] G. S. Winckelmans and A. Leonard. Contributions to vortex particle methods for the computation of 3-dimensional incompressible unsteady flows. *Journal Of Computational Physics*, 109(2):247–273, 1993.
[10] J. K. Salmon, M.S. Warren, and G.S. Winckelmans. Fast parallel tree codes for gravitational and fluid dynamical n-body problems. *Intl. J. Supercomput. Appl. High Perf. Comp.*, 8(2):192–142, 1994.
[11] E. Branlard, E. Machefaux, M. Gaunaa, H.H. Brandenborg Sørensen, and N. Troldborg. Validation of vortex code viscous models using lidar wake measurements and CFD. In *Proceedings*. EWEA - The European Wind Energy Association, 2014.
[12] Giorgos Papadakis. *Development of a hybrid compressible vortex particle method and application to external problems including helicopter flows*. PhD thesis, National Technical University of Athens, 2014.
[13] C. R. Anderson. A method of local corrections for computing the velocity field due to a distribution of vortex blobs. *Journal of Computational Physics*, 62(1):111–123, 1986.
[14] GT Balls and P. Colella. A finite difference domain decomposition method using local corrections for the solution of poisson's equation. *Journal Of Computational Physics*, 180(1):25–53, 2002.
[15] G.-H. Cottet and P. Koumoutsakos. *Vortex methods: theory and practice*. Cambridge University Press, 2000.
[16] T. J. Larsen and A. M. Hansen. *HAWC2 - User manual*. DTU-Risø-R-1597, 2007.
[17] J. G. Leishman and T.S. Beddoes. A semi-empirical model for dynamic stall. *Journal of the American Helicopter Society*, 34(3):p3–17, 1989.
[18] G. S. Winckelmans. *Encyclopedia of computational mechanics - Volume 1. Chapter 5: Vortex Methods*, chapter 5. J. Wiley & Sons, New-York, N.Y., 2004.

[19] E. Branlard and M. Gaunaa. Impact of a wind turbine on turbulence: un-freezing the turbulence by means of a simple vortex particle approach, 2015. (Submitted to the Journal of Wind Engineering and Industrial Aerodynamics, currently under review).
[20] P. Degond and S. Mas-Gallic. The weighted particle method for convection-diffusion equations. part 1: The case of an isotropic viscosity. *Mathematics of Computation*, 53(188):485–507, 1989.
[21] G. Daeninck. *Developments in hybrid approaches: Vortex method with known separation location Vortex method with near-wall Eulerian solver RANS-LES coupling*. PhD thesis, Université catholique de Louvain, Faculté des sciences appliiquées, 2006.
[22] S. G. Voutsinas. Vortex methods in aeronautics: how to make things work. *International Journal of Computational Fluid Dynamics*, 2006.
[23] M. J. M. Hill. *On a spherical vortex*. the Royal Society, 1894.
[24] D. G. Akhmetov. *Vortex rings*. Springer, 2009.
[25] J. T. Beale and A. Majda. High Order Accurate Vortex Methods with Explicit Velocity Kernels. *Journal of Computational Physics*, 208:188–208, 1985.
[26] M. N. Hejlesen, J. T. Rasmussen, P. Chatelain, and J-H. Walther. A high order solver for the unbounded poisson equation. *Journal of Computational Physics*, 252:458–467, 2013.
[27] J. T. Beale and A. Majda. Rates of convergence for viscous splitting of the navier-stokes equations. *Mathematics of Computation*, 37:243–259, 1981.
[28] H.Aa. Madsen, V. Riziotis, F. , Zahle, M.O.L. Hansen, H. Snel, F. Grasso, T.J. Larsen, E. Politis, and F. Rasmussen. Blade element momentum modeling of inflow with shear in comparison with advanced model results. *Wind Energy*, 15:63–81, 2012.
[29] F. Grasso. Ground and Wind Shear Effects in Aerodynamic Calculations. Technical Report ECN-E–10-016, Energy research center of the Netherlands (ECN), 2010.
[30] J. Mann. The spatial structure of neutral atmospheric surface-layer turbulence. *Journal of Fluid Mechanics*, 273:p141–168, 1994.
[31] J. T. Rasmussen, M. M. Hejlesen, A. Larsen, and J-H. Walther. Discrete vortex method simulations of the aerodynamic admittance in bridge aerodynamics. *Journal of Wind Engineering and Industrial Aerodynamics*, 98(12):754–766, 2010.
[32] S. Backaert, P. Chatelain, G. Winckelmans, and I. De Visscher. Vortex particle-mesh simulations of atmospheric turbulence effects on wind turbine blade loading and wake dynamics. In M. Hölling, J. Peinke, and S. Ivanell, editors, *Wind Energy - Impact of Turbulence*, volume 2 of *Research Topics in Wind Energy*, pages 135–140. Springer Berlin Heidelberg, 2014.
[33] D. Sale, A. Aliseda, and Y. Lic. Simulation of hydrokinetic turbines in turbulent flow using vortex particle methods. In *Proceedings of the 2nd Marine Energy Technology Symposium: METS2014-April 15-18, 2014, Seattle, WA*, 2014.
[34] N. Troldborg, J. N. Sorensen, and R. Mikkelsen. Actuator line simulation of wake of wind turbine operating in turbulent inflow. *Science Of Making Torque From Wind*, 75(1):–, 2007.
[35] A. S. Monin and A. M. Yaglom. *Statistical fluid mechanics mechanics of turbulence. vol. 1*. MIT press, Cambridge, 1971.
[36] G. K. Batchelor and A. A. Townsend. Decay of vorticity in isotropic turbulence. *Proceedings of the Royal Society of London A: Mathematical, Physical and Engineering Sciences*, 190(1023):534–550, 1947.
[37] T. de Kármán and L. Howarth. On the statistical theory of isotropic turbulence. *Proceedings of The Royal Society of London Series A-Mathematical And Physical Sciences*, 164(917):192–215, 1937.
[38] A. Thormann and C. Meneveau. Decay of homogeneous, nearly isotropic turbulence behind active fractal grids. *Physics of Fluids*, 26(2):1, 2014.
[39] E. Branlard, M. Gaunaa, and E. Machefaux. Investigation of a new model accounting for rotors of finite tip-speed ratio in yaw or tilt. *Journal of Physics: Conference Series (Online)*, 524(1), 2014.
[40] N. Troldborg, J. N. Sørensen, R. F. Mikkelsen, and N. N. Sørensen. A simple atmospheric boundary layer model applied to large eddy simulations of wind turbine wakes. *Wind Energy*, 17(4):657–669, 2014.
[41] Frederik Zahle and Niels Sørensen. Rotor aerodynamics in atmospheric shear flow. *EWEC 2008 Conference Proceedings*, pages 120–124, 2008.
[42] M. Gaunaa, N. Troldborg, and E. Branlard. Modelling the influence of wind shear using a simple vortex rotor model, 2015. (To appear in *Wind Energy*).